Precipitation of monodisperse ZnO nanocrystals *via* acid-catalyzed esterification of zinc acetate

Mustafa M. Demir, Rafael Muñoz-Espí, Ingo Lieberwirth and Gerhard Wegner*

Received 30th January 2006, Accepted 10th May 2006
First published as an Advance Article on the web 2nd June 2006
DOI: 10.1039/b601451h

A wet-chemical method to produce zinc oxide nanocrystals of monodisperse size distribution (diameter range of 20–80 nm) is presented. The synthesis starts from zinc acetate dihydrate which is converted to ZnO in the presence of 1-pentanol in *m*-xylene at 130 °C. We report for the first time catalysis of this reaction by *p*-toluene sulfonic acid monohydrate (*p*-TSA), which allows a shorter reaction time and improves both the reproducibility of the particle size distribution and the crystallinity of the particles. The reaction can be scaled up to give multigram quantities of product per batch. Particles were characterized by X-ray diffractometry (XRD), scanning electron microscopy (SEM), high-resolution transmission electron microscopy (HRTEM), and photoluminesence (PL) spectroscopy. Room temperature PL spectra of ZnO prepared without catalyst exhibit a strong and sharp UV emission band at *ca.* 385 nm and a weak and very broad green–yellow visible emission centered at *ca.* 550–560 nm. However, for nanoparticles precipitated in the presence of *p*-TSA, the UV emission is enhanced by a factor of 4, which can be correlated with the improvement of crystal perfection. A particle formation mechanism is discussed.

Introduction

Besides its conventional uses in paints, cosmetics, catalysis, and gas sensors, zinc oxide appears to be a promising material for optoelectronic devices, such as light emitting diodes in the blue-to-UV region, flat display screens, and solar cells.[1] These advanced applications require well-defined crystals in the submicron range. Therefore, the scientific activity devoted to the synthesis and characterization of ZnO structures has increased incredibly over the past years. Numerous chemical strategies have been reported to synthesize micro- and nanoscaled ZnO, including controlled precipitation,[2–4] hydrothermal[5,6] and solvothermal methods,[7,8] sol–gel,[9–13] thermal decomposition of precursors,[14,15] laser ablation,[16] spray pyrolysis,[17] oxidation of zinc metal,[18] and microemulsion.[19] However, the preparation of monodisperse nanocrystals with homogeneous properties in large volumes still remains a challenge.[20]

Among the mentioned synthetic routes, wet-chemical processes have been widely recognized as an efficient approach to prepare nanocrystalline particles, and may be scaled up to produce large quantities.[21] For instance, Cozzoli *et al.*[22] presented a scalable non-hydrolytic route to produce ZnO nanocrystals by means of thermal decomposition of zinc acetate in a mixture of alkylamine and *t*-butyl phosphonic acid. Another recent example was given by Pinna *et al.*,[23] who proposed a solvothermal route based on the reaction between zinc acetylacetonate and benzyl amine with a particle formation mechanism encompassing solvolysis of acetylacetonate.

Max Planck Institute for Polymer Research, Ackermannweg 10, D-55116 Mainz, Germany. E-mail: wegner@mpip-mainz.mpg.de; Fax: +49 6131 379 330; Tel: +49 6131 379 130

The majority of studies on the preparation of ZnO nanoparticles by wet-chemical methods at low temperature have been mainly directed towards sol–gel processes, which seem to be very attractive because they are relatively easy to carry out. Typically, this synthetic method involves the hydrolysis of zinc salts with strong bases (*e.g.*, NaOH, LiOH, KOH, or tetramethylammonium hydroxide) as an oxygen source in an alcoholic medium, and the polycondensation of metastable $Zn(OH)_2$ into ZnO crystals. The major problem of sol–gel routes is the uncontrolled reaction rates of the hydrolysis and condensation steps, resulting in the formation of precipitates with a high degree of structural defects.[11] The incorporation of alkali ions may result in the creation of crystal defects that can strongly affect the physical properties of the crystals, especially the luminescence efficiency, because of the increase of non-radiative recombination.[24]

In contrast to methods with *ex situ* introduction of hydroxyl ions into the reaction system, a synthetic route controlling the release of the oxygen donor as a product of a homogenous reaction would allow the preparation of nanoparticles with a low density of defects. This type of approach was reported for the synthesis of nanocrystalline anatase and rutile.[25,26] Titanium salts were hydrolyzed with water, generated *in situ* by the esterification of acetic acid with alcohols. The gradual release of water controls the rate of the hydrolysis reaction. Using the same esterification reaction, Du *et al.*[27] extended this approach to produce ZnO nanocrystals by reacting zinc acetate dihydrate with ethanol. The reaction, whose main novelty was the application of the esterification of a zinc salt itself, was performed at 120 °C under solvothermal conditions for 24 h. Recently, Joo *et al.*[28] obtained anisotropic ZnO nanoparticles of various shapes using the solvothermal esterification between zinc acetate dihydrate and 1,12-dodecanediol in the presence of surfactants. The diol was selected

because of its reasonable reaction rate with zinc acetate, and the reaction was maintained at above 200 °C for 2 h.

In the present work, we describe a chemical precipitation process to obtain ZnO nanoparticles of high crystal perfection through acid-catalyzed esterification of zinc acetate dihydrate ($Zn(AcO)_2{\cdot}2H_2O$) with 1-pentanol at 130 °C. In our process, contrasting from the methods previously mentioned, the liquid-phase esterification is performed under reflux in the presence of acid catalysts. The time to completion of nucleation and growth is relatively fast in comparison to the reported solvothermal routes. The effects of *p*-toluene sulfonic acid (*p*-TSA), which is a very effective catalyst, on reaction rate, particle morphology (shape and size), and optical properties are investigated. The use of an alternative catalyst, $ZnBr_2$, is also examined.

Experimental

Synthesis of ZnO nanoparticles

Nanosized zinc oxide was prepared by refluxing zinc acetate dihydrate ($Zn(AcO)_2{\cdot}2H_2O$, Aldrich, ACS grade) in a mixture of 1-pentanol (Acros, 99%) and *m*-xylene (Acros, 99+%). *m*-Xylene was used as a high boiling point diluent. For a typical synthesis, *p*-toluene sulfonic acid monohydrate (*p*-TSA, Merck, p.a.) was dissolved in a mixture of *m*-xylene (25 mL) and 1-pentanol (50 mL). 2.5 g of $Zn(AcO)_2{\cdot}2H_2O$ were added to the solution and this mixture was refluxed at 140 °C (temperature of the oil bath, 130 °C inside the reactor). $Zn(AcO)_2{\cdot}2H_2O$ dissolved completely within the first ten min of refluxing. Eventually, the solution turned into a milky suspension. The white precipitate was separated by centrifugation at 4000 rpm for 10 min, and then rinsed several times with ethanol and distilled water. The solvents were evaporated under reduced pressure at 40 °C and a white powder was obtained. Because the rate of esterification is enhanced in excess alcohol,[29] 1-pentanol was used in an excess of a factor of 20 with regard to the zinc salt.

Characterization techniques

Scanning electron microscopy (SEM) was performed on dry powders without sample sputtering with a LEO Gemini 1530 field-emission microscope, operating at an accelerating voltage of 1 kV, a working distance of 2 mm, and an aperture size of 30 μm. Particle size distributions were obtained from statistical treatment of SEM images by measuring the length of typically not less than 300 particles with help of the software Image J.[30] High-resolution transmission electron microscopy (HRTEM) was carried out with a FEI Tecnai F-20 microscope working at a voltage of 200 kV.

X-Ray diffractograms were registered in a Seifert XRD 3000 TT diffractometer by using a Cu Kα radiation source (λ = 0.15418 nm).

Raman spectra were measured from the powders in a Bruker RFS100 spectrometer equipped with a laser source (1064 nm, 510 mW), working with a power of 450 mW.

UV–visible absorption spectra were measured by a Perkin Elmer Lambda 2 spectrometer. Photoluminescence spectra were recordered under ambient conditions by a Spex Fluorolog 212 spectrometer, equipped with a Xe lamp. Dispersions of the samples in ethanol (Fisher Scientific, HPLC grade) were prepared with a concentration of *ca.* 1 mg mL^{-1} by ultrasonication. The spectra of these dispersions were measured using a quartz cell having a path length of 10 mm. In case of the solid-state measurements, a specially designed cell was used, comprised of two quartz plates placing the powder sample in between. Emission spectra were recorded using an excitation wavelength of 310 nm; an emission wavelength of 560 nm was fixed for the excitation spectra. A 345-nm edge filter was used and the scanning velocity was of 2 nm s^{-1}. For dynamic studies, the detection wavelengths were fixed at 385 ± 1 and 560 ± 1 nm. A time of not less than 3 min without irradiation elapsed between the different measurements, to allow the complete relaxation of the samples.

Luminescence quantum yields were measured following a standard procedure[31] by comparing the integrated emission intensities of reference solutions of 9,10-diphenylanthracene (Riedel-de-Haën, 99.8%) in cyclohexane (Fisher Scientific, HPLC grade) and ethanolic suspensions of the prepared ZnO particles (different concentrations lower than 0.1 mg mL^{-1}).

Results and discussion

I. Morphological and structural characterization

ZnO nanoparticles were precipitated in the mixture 1-pentanol–xylene in the absence and presence of *p*-toluene sulfonic acid (*p*-TSA). Fig. 1 shows the scanning electron microscopy (SEM) and high-resolution transmission electron microscopy (HRTEM) images of particles obtained at 130 °C after a reaction time of 2 h. Samples obtained with and without *p*-TSA appear to be similar, although the particle size distributions are different, as will be discussed below. In both cases, the particles are small, with an average size below 50 nm, non-agglomerated, and ellipsoidal. HRTEM micrographs of single particles confirmed the hexagonal structure and display

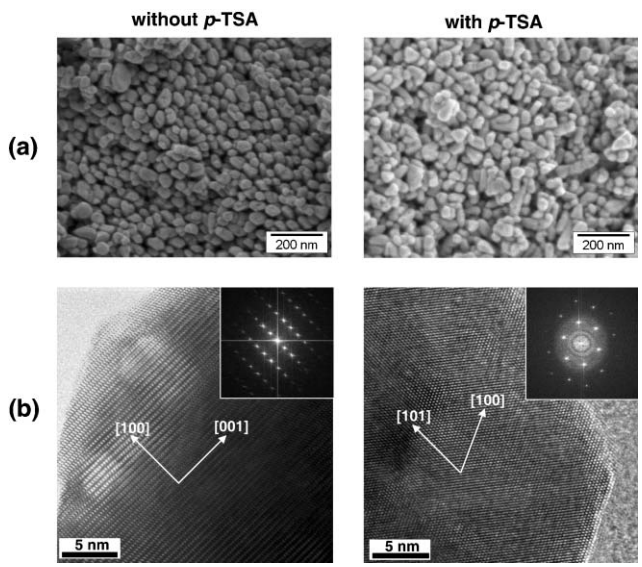

Fig. 1 (a) SEM and (b) HRTEM images of ZnO nanoparticles prepared in 2 h at 130 °C, in the absence and presence of *p*-TSA (0.013 mol L^{-1}).

the lattice fringes of zincite. No significant differences were observed in the perfection of the crystals.

Further analysis of the crystal structure of the products was performed by X-ray diffraction (XRD). Fig. 2 presents the XRD patterns of representative samples obtained without catalyst (reaction times of 1 and 2 h) and with *p*-TSA (0.013 mol L^{-1} and 1 h reaction). Without catalyst, the 1 h reaction product appears to be a mixture of anhydrous zinc acetate (JCPDS card No. 1–89) and zincite (JCPDS card No. 36–1451), whereas only zincite can be identified in the product obtained after 2 h. The sharp diffraction peaks point towards the perfection of the particles. The disappearance of the anhydrous $Zn(AcO)_2$ reflections suggests that this species is an intermediate product in the precipitation reaction. In the presence of *p*-TSA, under the same experimental conditions, $Zn(AcO)_2$ reflections do not appear and zincite is the only phase found after 1 h. These observations confirm the catalytic effect of *p*-TSA, since the necessary time to complete the reaction (*i.e.*, only zincite is present in the product) is shortened.

Assuming that the broadening of XRD peaks results only from the size of the coherently scattering domains, their size (referred as crystallite size or coherence length) can be estimated by the Scherrer formula,[32] $L_{hkl} = K\lambda/(\beta_{1/2}\cos\theta)$, where K is a form factor approximately equal to unity, λ is the radiation wavelength (0.154 nm for Cu Kα radiation), and $\beta_{1/2}$ is the full width at half maximum (FWHM) of the peak on the 2θ scale in radians. Table 1 contains the coherence lengths corresponding to (100) and (002), when applying the Scherrer formula to these reflections in samples obtained with different *p*-TSA concentrations after different reaction times. L_{002} is slightly but systematically larger than L_{100} for all samples, which may be explained by the fact that growth in the direction [001] is faster than in [100]. When samples prepared at different reaction times are compared, the coherence lengths become larger with increasing time. The *p*-TSA concentration has a minor effect on L_{hkl}, since the differences are only within the range of experimental error.

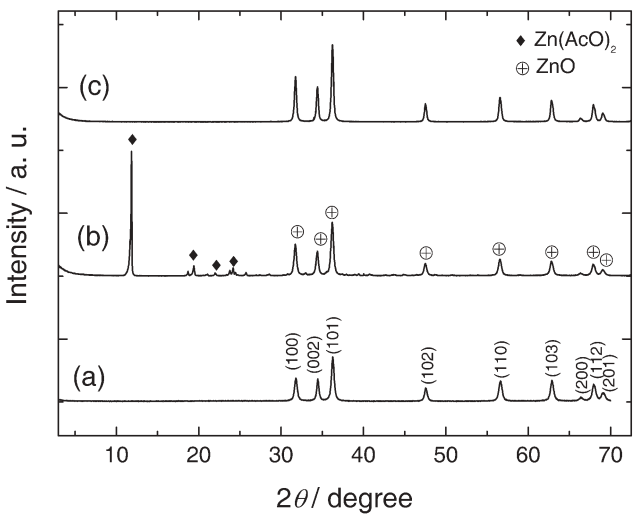

Fig. 2 XRD patterns of products obtained at 130 °C: (a) after 2 h without *p*-TSA; (b) after 1 h without *p*-TSA; and (c) after 1 h in the presence of 0.013 mol L^{-1} of *p*-TSA. The concentration of zinc salt was 0.15 mol L^{-1}.

Table 1 Values of the average crystallite sizes calculated from the (100) and (002) XRD reflections as a function of *p*-TSA concentration and reaction time

[*p*-TSA]/mol L^{-1}	Reaction time/h	L_{100}/nm	L_{002}/nm
0	1	25	26
0	2	31	32
0	3	35	37
0.013	1	24	29
0.013	2	31	40
0.013	3	31	37
0.026	3	30	37
0.052	3	29	40

For many applications of semiconductor particles, especially those concerning optical transparency, a narrow particle size distribution (PSD) is crucial.[33] Therefore, the shape and width of PSD as a consequence of the preparation conditions have to be controlled. Two parameters influence the particle size and PSD: reaction time and catalyst concentration. Crystal sizes were studied by analyzing the size distributions obtained by the statistical treatment of particle lengths from SEM images. Fig. 3a presents the PSD of samples prepared isothermally at different reaction times. It is observed that ZnO particles become larger and PSD becomes broader with increasing reaction time. This feature can be rationalized considering that the growth of the particles occurs by Ostwald ripening, mediated by the presence of *p*-TSA in the reaction medium. To obtain nanoparticles of narrow size distribution, one should provide a homogenous reaction medium that does not exhibit a temperature or solute concentration gradient. Therefore, stirring the solution during the reaction is extremely important. Fig. 3b shows the size distributions of the particles precipitated from solutions with different *p*-TSA concentrations, adjusted at the beginning of the reaction. The particles obtained in the presence of catalyst are smaller and exhibit a narrower distribution. The crystal dimensions measured from SEM are comparable to the coherence lengths calculated by the Scherrer formula. This indicates that the particles are single crystals and the particle growth occurs through Ostwald ripening rather than through aggregation of individual particles.

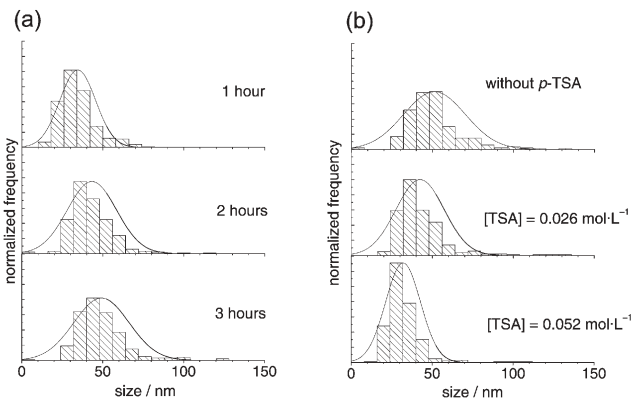

Fig. 3 Size distributions of particles obtained at 130 °C: (a) after different reaction times at a constant *p*-TSA concentration of 0.013 mol L^{-1}; (b) at different *p*-TSA concentrations after a constant reaction time of 3 h.

Two possible roles of *p*-TSA affecting the particle morphology can be considered. First, the narrowing of the size distribution as a result of increasing acid concentration can be ascribed to the catalytic effect of *p*-TSA. The nucleation might be catalyzed by reducing the free-energy barrier needed to create a nucleus of critical size. As the catalyst concentration increases, more and more nuclei form per unit time. Thus, increasing amounts of smaller particles with a narrower size distribution are obtained, whereas particles prepared without catalyst are larger and show a broader size distribution. Second, *p*-TSA could also act as a terminating agent by coordinating to the surface of the particles. The chelation between sulfonic acid and the zinc atom(s), if existing in the system, might have somewhat of a stabilizing effect and may moderate the reaction between the alcohol and zinc acetate. The ability to control the ZnO nucleation and growth can be related to the nature of the complexation of Zn atoms (both in the precursor and on the particle surface) during the particle growth. Nevertheless, one should take into account that *p*-TSA is a strong acid; the acidic medium improves the solubility of ZnO in alcoholic solution, and it has a negative effect on the product yield. While the yield was 87 $\pm$ 6% in the absence of catalyst, it decreases to 69 $\pm$ 9% because of high solubility of ZnO-derived products when *p*-TSA is present.

p-TSA is a homogenous esterification catalyst, in the sense that it is miscible with the reaction medium. Although *p*-TSA may coordinate zinc atoms, it can be removed from the product by simple washing with distilled water. The removal of catalyst from the particle surface was demonstrated by Raman spectra of the particles before and after the washing procedure with distilled water. The ν(SO) and $\nu(SO_3^-)$ stretching bands, appearing at 1125 and 1037 cm^{-1}, respectively,[34] disappear after the washing procedure. This result also indicates that insoluble zinc tosylate was not formed.

Another typical esterification reaction catalyst, $ZnBr_2$, was applied to the system to investigate its effect on the particle formation. $ZnBr_2$ is a Lewis acid and, as is *p*-TSA, a homogeneous catalyst, because of its solubility in the mixture of 1-pentanol and xylene. For the comparison of these two catalysts, two reactions were run, keeping all the reaction parameters constant. It was found that $ZnBr_2$ promotes the reaction to produce pure ZnO; however, SEM images show that the desired particle morphology of non-aggregated crystals was not achieved. Fig. 4 shows SEM images of these samples, obtained after 1 h in the presence of 0.013 mol L^{-1} of either *p*-TSA or $ZnBr_2$. ZnO produced under *p*-TSA catalysis shows spherical and ellipsoidal *ca.* 30-nm particles with well-defined shape. Surprisingly, in the presence of $ZnBr_2$, the sample contains large aggregates, including hexagonal- and bipyramidal-shaped crystals of zincite. While homogenous particle morphology is achieved both in the absence and presence of *p*-TSA, the morphology becomes heterogeneous when $ZnBr_2$ is introduced into the system. The presence of $ZnBr_2$ provides a new zinc source in the reaction medium and leads to the formation of larger aggregates. The specific mechanism that causes these morphological differences remains unclear, but a nucleating effect of $ZnBr_2$ could be supposed.

II. Photoluminescence

Photoluminescence (PL) excitation and emission spectra, shown in Fig. 5, were measured at room temperature for ethanolic suspensions of different samples synthesized without and with *p*-TSA, and at different reaction times. The suspensions were stable for a longer period of time than required for measurement.

Spectra of the samples in the solid state (*i.e.*, directly from the powder samples) were also registered. In this case, the samples were prepared by placing the powders between two quartz plates of a specially designed cell. We are aware that in this experimental procedure, the pressure exerted on the samples could be slightly different due to the different powder textures. However, since the preparation method was similar and the samples have approximately the same density (a maximum weight loss up to 1.5 wt% was determined by thermogravimetrical analysis for the different samples), we are confident that the measurements are qualitatively comparable. The spectra were similar, within the limits of experimental error, and showed a comparable tendency to those registered for ethanolic suspensions.

Excitation spectra, recorded at an emission wavelength of 560 nm, are similar for all samples and present a pronounced peak placed at around 378 nm (3.28 eV). Emission spectra (λ_{exc} = 310 nm) show always a sharp UV peak at 385–386 nm (3.21–3.22 eV), which has a Stokes shift of 7–8 nm with respect to the excitation peak, and a very broad green-yellow visible band, less intense and centered at around 550–560 nm (2.21–2.25 eV). The UV peak appears to be quite narrow (FWHM of 11–12 nm for all our samples), with respect to typical values reported in literature for ZnO obtained in liquid phase.[9,35,36] The narrowness can be related to the nearly monodisperse size of the crystals. The visible PL band can be fitted relatively well

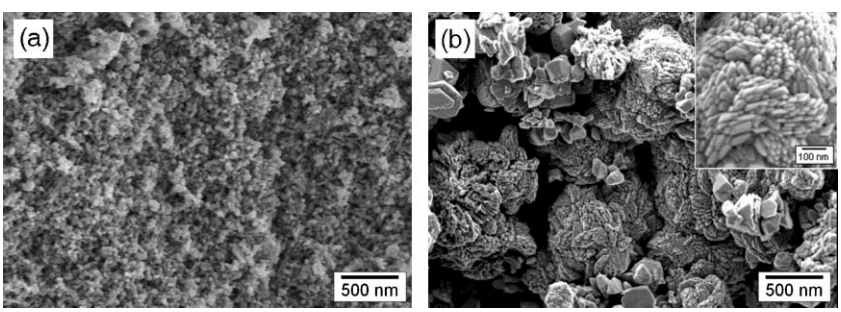

Fig. 4 SEM images of particles prepared in 1 h at 130 °C, in the presence of 0.013 mol L^{-1} of (a) *p*-TSA and (b) $ZnBr_2$.

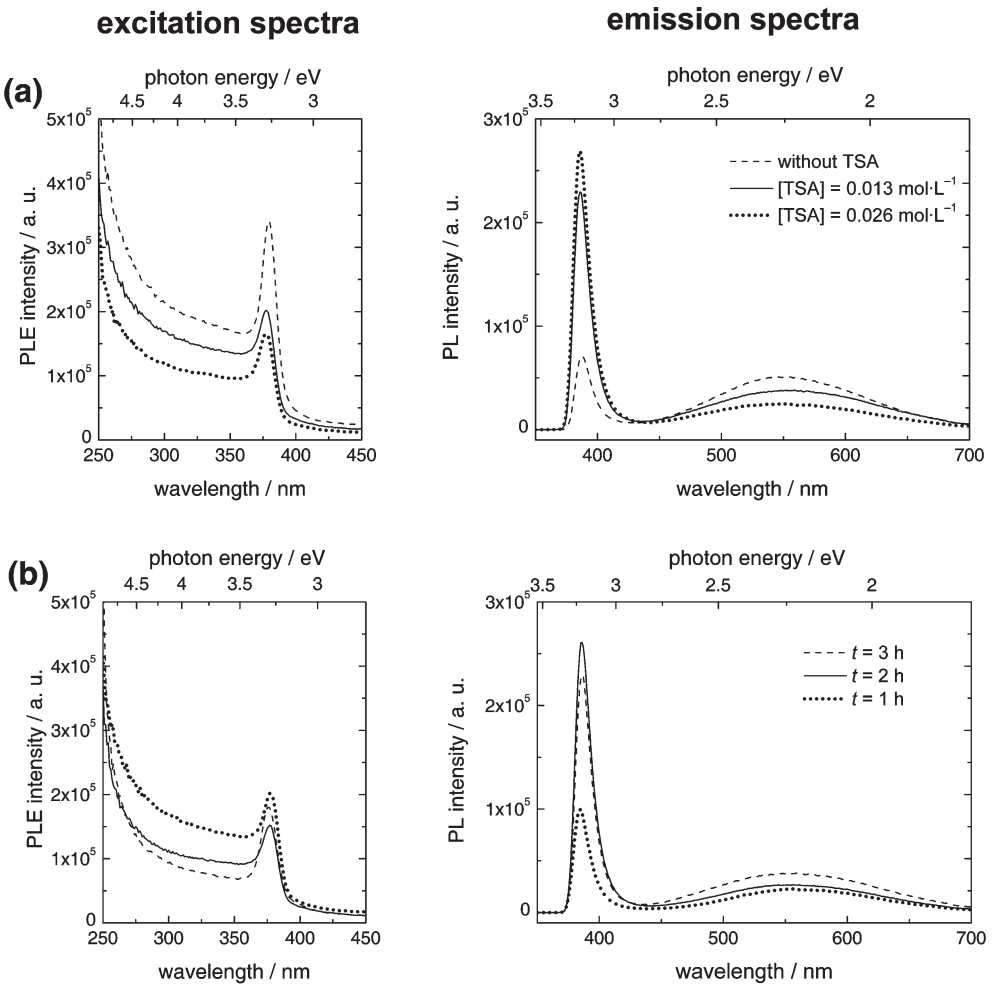

Fig. 5 Excitation (λ_{em} = 560 nm) and emission (λ_{exc} = 310 nm) PL spectra of ZnO suspensions: (a) synthesized in the absence and in the presence of *p*-TSA (0.013 and 0.026 mol L^{-1}) for a reaction time of 3 h; (b) synthesized at a fixed *p*-TSA concentration of 0.013 mol L^{-1} for different reaction times.

to a simple Gaussian curve, although the fitting improves slightly with two Gaussians. This might suggest more than one contribution to the visible emission, probably of different physical origins.

Although the two bands are present in all the samples, their intensities and ratio change significantly. In Fig. 5a, spectra of samples prepared in the absence and in the presence of *p*-TSA are compared, keeping the reaction time (3 h) constant. In the absence of *p*-TSA, both the UV and visible emissions have a similar intensity: the maximum intensity of the UV peak is only a factor of *ca.* 1.5 higher than the intensity of the peak in the visible. The addition of *p*-TSA clearly leads to a significant enhancement of the UV peak, up until a factor of 4 (in regard to the sample synthesized without additive), parallel to a quenching of the visible emission. Considering the maxima, the UV emission for [*p*-TSA] = 0.013 mol L^{-1} is a factor of 6 more intense than the visible, for [*p*-TSA] = 0.026 mol L^{-1} the difference increases to almost a factor of 11. In Fig. 5b, the influence of the reaction time on the PL spectra is shown, keeping the concentration of *p*-TSA (0.013 mol L^{-1}) constant. The UV-to-visible intensity ratio is 4.5 after 1 h and increases until *ca.* 10 after 2 h. In case of the 3-h sample, this ratio decreases slightly, which may be caused by the formation of higher amounts of crystal defects at longer reaction times.

The presence of *p*-TSA also showed an improvement in the overall luminescence quantum yield (*i.e.*, ratio of the emitted photons to the absorbed ones), Φ, estimated by comparing our ethanolic suspensions with solutions of a reference (9,10-diphenylanthracene in cyclohexane, Φ = 0.95).[31] The quantum yield for the particles prepared in 3 h without catalyst is 0.0094. This value is more than doubled, Φ = 0.0193, for the particles precipitated at [*p*-TSA] = 0.026 mol L^{-1}. For lower catalyst concentrations and lower reaction times, the quantum yield is in between these two values. Semiconductor suspensions show typically low quantum yields,[9,37–39] which is explained by strong scattering and radiationless energy dissipation. The efficiency of the luminescence of such suspensions depends on many conditions, the size and the nature of the surface being especially important. In case of ZnO colloidal suspensions, van Dijken *et al.*[40] reported an increase in the quantum efficiency of the visible emission from 0.12 to 0.20 when the particle size decreases from 1 to 0.7 nm (the UV emission is neglected by the authors in the determination of the luminescence efficiency). In another

article, Bahnemann *et al.*[9] reported an overall quantum yield of 0.03 for 5-nm particles. In the present work, although the particle size is one order of magnitude larger and the scattering must be significantly higher,[41] quantum yields are comparable to those reported in the latter article.

Under the continuous monochromatic light of the spectrometer, a dynamic behavior of the PL emission was observed. The same effect appeared for samples prepared with and without *p*-TSA. This is illustrated by Fig. 6, where it is shown that the visible emission decreases up to *ca.* 35% after several seconds, while the UV emission increases simultaneously up to *ca.* 45%. After 40–45 s, the emission intensities remain approximately constant. The process was found to be reversible and the curves are reproducible, if the measurements are taken with a difference of few minutes to allow the complete relaxation of the samples. Since the whole time to register a spectrum is around 3 min (scanning velocity of 2 nm s^{-1}) and the change in the intensity after several seconds is only a small percentage, the spectra presented in Fig. 5 are assumed to show the situation of equilibrium of the mentioned dynamic process. The shape of the curves shown in Fig. 6 and the reversibility of the process suggest a photo-induced desorption of species adsorbed on the surface of the nanoparticles, presumably oxygen from the medium. Bahnemann *et al.*[9] attributed a similar observation to a photodesorption of molecular oxygen strongly chemisorbed to the surface of zinc oxide, which is assumed to be involved in the PL emission.

The explanation of the experimental observations requires the understanding of the origin of the photoluminescence in ZnO. Whereas most authors agree to attribute the UV emission to exciton annihilation, the origin of the visible emission is more controversial and has been investigated for decades. Many contradictions are found in the literature: visible bands at different positions, attributed to different crystal defects and involving different mechanisms, have been reported. Bahnemann *et al.* suggested a model that considers

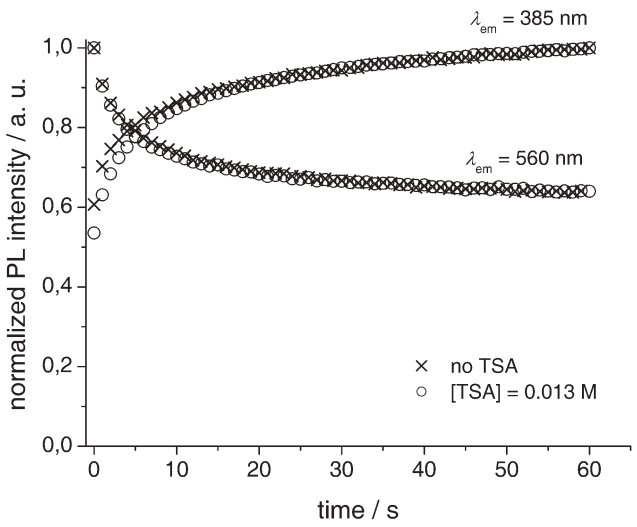

Fig. 6 Dynamic behavior of the UV and visible PL emission (λ_{exc} = 310 nm) for samples prepared in the absence and in the presence of *p*-TSA (0.013 mol L^{-1}).

the preexistence of electron traps in the sample, probably associated to crystal defects. After photoexcitation, hole–electron pairs are generated, and three competing processes are possible: (i) non-radiative relaxation, (ii) radiative exciton recombination, and (iii) trapping of photogenerated electrons, followed by the radiative transition to the valence band. The low quantum yields obtained indicate that the first process is dominant. The second process is responsible for the sharp UV peak, while the last one originates the visible emission. Oxygen species adsorbed to the surface, with a tendency to accept electrons, seem to mediate the transition of the photogenerated electron from the conduction band to the "trap". When these species are photodesorbed, visible emission decreases and, due to the competing nature of the processes, the exciton recombination becomes more probable and the UV emission is enhanced.

An alternative mechanism to explain the visible emission, but also involving oxygen species at surface positions, has been proposed by van Dijken *et al.*[42] They assigned the green band to the radiative transition of an electron from the conduction band to doubly ionized oxygen vacancies ($V_O^{\bullet\bullet}$), resulting from the tunneling of a photogenerated hole, trapped at the surface, to a singly ionized $V_O^{\bullet}$ center.

Independently of the physical mechanism behind the visible emission, it can pointed out that our samples show a weak visible emission in all cases, in contrast to the intense emissions reported when strong bases, such as LiOH,[42,43] NaOH,[9,44] or KOH,[36] are used. This can be explained by a decrease in the amount of structural defects due to the *in situ* release of water as the oxygen source in the esterification reaction. The observed enhancement of the UV emission in the presence of *p*-TSA must be related to the reduction or "deactivation" of centers that cause non-radiative recombination or visible emission. Assuming (as is correct) that surface species play a crucial role in photoluminescence, the presence of *p*-TSA in the synthesis may have caused a higher perfection of the crystal surface producing less vacancies or excess sites.

III. Mechanism of particle formation

A possible reaction mechanism can be proposed on the basis of the experimental results. The formation of zincite nanoparticles is mainly based on a hydrolytic process initiated by the OH^- ions, generated as a result of an esterification reaction of acetate ions with 1-pentanol. We assume that the hydrolysis of $Zn(AcO)_2{\cdot}2H_2O$ is the first step of the overall reaction. Alcohols provide an appropriate medium for the hydrolysis of carboxylates that yield ZnO through the condensation route.[45] The esterification leads to the release of hydroxyl groups that bind to the zinc species. The generation of pentyl acetate was confirmed by ^{13}C NMR analysis of the supernatant solution, after the ZnO particles had been removed. The condensation of the zinc hydroxyl species occurs under elimination of water, resulting in the formation of Zn–O–Zn bonded species. The nucleation can be achieved by further cycles of esterification and subsequent condensation reactions to give clusters, which may still be dissolved in the reaction medium. The nucleation is accomplished when the number of ZnO units per cluster exceeds a

threshold that leads to the critical size of the nucleus. *p*-TSA acts as an efficient promoter of particle formation, including both nucleation and growth steps. The esterification can be considered as the initiation step; the catalyst accelerates the reaction and, therefore, the nucleation of the crystals. In the growth step, the catalyst may also coordinate to the zinc atoms; a possible spurious formation of zinc toluene sulfonate that is soluble in the reaction medium could assist in the exchange of zinc species among the particles and mediate the particle growth.

ZnO crystals can be formed either directly by homogeneous precipitation, or through redissolution of metastable hydroxo-intermediates, such as zinc hydroxide or zinc hydroxyacetate that change into the more stable zincite. Layered zinc hydroxyacetates have been obtained in near room temperature processes from $Zn(AcO)_2$ in alcoholic media,[46,47] but these species should be unstable at the reaction temperature of 130 °C. In general, all $Zn(OH)_2$ polymorphs are more soluble and less stable than ZnO.[48] Crystallization in the presence of organic additives may stabilize zinc hydroxide intermediate phases.[49] However, in our experiments, the crystal structure was always confined to zincite in the absence/presence of the *p*-TSA. We assume that $Zn(OH)_2$, if it exists at all under our reaction conditions, has a very short lifetime and is converted rapidly into ZnO.

Conclusions

Zinc oxide nanocrystals of 25–50-nm mean size were synthesized in the course of the acid-catalyzed transesterification of zinc acetate dihydrate with 1-pentanol. In comparison to other reported methods, such as solvothermal synthesis, this pathway presents several advantages: (i) less complex equipment (reflux) and inexpensive chemicals are used; (ii) nanoparticles can be synthesized in a short time (1–2 h) on the gram scale, at atmospheric pressure and relatively low temperature (130 °C); and (iii) organic additives can be applied during and after the particle formation to control surface properties and particle size.

Two different acid catalysts were used: *p*-toluene sulfonic acid (*p*-TSA) and $ZnBr_2$. The former was shown to work efficiently in the sense that it helped to produce monodisperse particle sizes of non-aggregated crystals, whereas the latter was not effective in our system and it resulted in a complex morphology. *p*-TSA not only accelerates the esterification reaction, but also leads to smaller and monodisperse crystals, without affecting significantly the morphology and the long-range crystal order, as proved by electron microscopy and X-ray diffraction. The catalyst seems to produce a higher number of nucleation sites in shorter time; thus, the particle size can be tuned by changing the *p*-TSA concentration and the reaction time.

A narrow UV peak, significantly enhanced when *p*-TSA was used as catalyst, and a very broad green-yellow band appear in the photoluminescence (PL) spectra. The former is attributed to near-band-edge exciton recombination, whereas the latter can be related to trapped-electron emission. The enhancement of the UV peak and the suppression of visible emission point towards a good crystallinity and a low density of structural defects in the nanoparticles synthesized in the presence of the catalyst.

It is worth mentioning that ZnO particles prepared under *p*-TSA catalysis are well suited to prepare hybrid polymer/ZnO composites by polymerizing mixtures of the particles with monomers such as methylmethacrylate.[50]

Acknowledgements

M. Steiert, C. Sieber, and H. Menges are thanked for technical assistance. The Max Planck Society is acknowledged for financial support.

References

1 C.-H. Yan, J. Zhang and L.-D. Sun, in *Encyclopedia of Nanoscience and Nanotechnology, vol. 10*, ed. H. S. Nalwa, American Scientific Publishers, Stevenson Ranch, 2004, pp. 767–780.
2 M. Öner, J. Norwig, W. H. Meyer and G. Wegner, *Chem. Mater.*, 1998, **10**, 460–463.
3 A. P. A. de Oliveira, J. F. Hochepied, F. Grillon and M. H. Berger, *Chem. Mater.*, 2003, **15**, 3202–3207.
4 R. Muñoz-Espí, Y. Qi, I. Lieberwirth, C. M. Gómez and G. Wegner, *Chem.–Eur. J.*, 2006, **12**, 118–129.
5 B. Liu and H. C. Zeng, *J. Am. Chem. Soc.*, 2003, **125**, 4430–4431.
6 X. M. Sun, X. Chen, Z. X. Deng and Y. D. Li, *Mater. Chem. Phys.*, 2003, **78**, 99–104.
7 L. Yang, G. Z. Wang, C. J. Tang, H. Q. Wang and L. Zhang, *Chem. Phys. Lett.*, 2005, **409**, 337–341.
8 S. H. Yu, J. Yang, Y. T. Qian and M. Yoshimura, *Chem. Phys. Lett.*, 2002, **361**, 362–366.
9 D. W. Bahnemann, C. Kormann and M. R. Hoffmann, *J. Phys. Chem.*, 1987, **91**, 3789–3798.
10 L. Spanhel and M. A. Anderson, *J. Am. Chem. Soc.*, 1991, **113**, 2826–2833.
11 M. S. Tokumoto, S. H. Pulcinelli, C. V. Santilli and V. Briois, *J. Phys. Chem. B*, 2003, **107**, 568–574.
12 E. A. Meulenkamp, *J. Phys. Chem. B*, 1998, **102**, 5566–5572.
13 D. Mondelaers, G. Vanhoyland, H. Van den Rul, J. D'Haen, M. K. Van Bael, J. Mullens and L. C. Van Poucke, *Mater. Res. Bull.*, 2002, **37**, 901–914.
14 Z. J. Wang, H. M. Zhang, L. G. Zhang, J. S. Yuan, S. G. Yan and C. Y. Wang, *Nanotechnology*, 2003, **14**, 11–15.
15 S. C. Pillai, J. M. Kelly, D. E. McCormack, P. O'Brien and R. Ramesh, *J. Mater. Chem.*, 2003, **13**, 2586–2590.
16 H. Usui, Y. Shimizu, T. Sasaki and N. Koshizaki, *J. Phys. Chem. B*, 2005, **109**, 120–124.
17 S. A. Studenikin, N. Golego and M. Cocivera, *J. Appl. Phys.*, 1998, **83**, 2104–2111.
18 Z. Zhang, H. Yu, X. Shao and M. Han, *Chem.–Eur. J.*, 2005, **11**, 3149–3154.
19 L. Guo, Y. L. Ji, H. B. Xu, P. Simon and Z. Y. Wu, *J. Am. Chem. Soc.*, 2002, **124**, 14864–14865.
20 O. Masala and R. Seshadri, *Annu. Rev. Mater. Res.*, 2004, **34**, 41–81.
21 X. Feng and M. Z. Hu, in *Encyclopedia of Nanocience and Nanotechnology, vol. 10*, ed. H. S. Nalwa, American Scientific Publishers, Stevenson Ranch, 2004, pp. 687–726.
22 P. D. Cozzoli, M. L. Curri, A. Agostiano, G. Leo and M. Lomascolo, *J. Phys. Chem. B*, 2003, **107**, 4756–4762.
23 N. Pinna, G. Garnweitner, M. Antonietti and M. Niederberger, *J. Am. Chem. Soc.*, 2005, **127**, 5608–5612.
24 Z. Hu, D. J. Escamilla Ramírez, B. E. Heredia Cervera, G. Oskam and P. C. Searson, *J. Phys. Chem. B*, 2005, **109**, 11209–11214.
25 M. Ivanda, S. Music, S. Popovic and M. Gotic, *J. Mol. Struct.*, 1999, **481**, 645–649.
26 C. Wang, Z. X. Deng and Y. D. Li, *Inorg. Chem.*, 2001, **40**, 5210–5214.
27 H. C. Du, F. L. Yuan, S. L. Huang, J. L. Li and Y. F. Zhu, *Chem. Lett.*, 2004, **33**, 770–771.
28 J. Joo, S. G. Kwon, J. H. Yu and T. Hyeon, *Adv. Mater.*, 2005, **17**, 1873–1877.

29 M. Aslam and G. P. Torrence, in *Encyclopedia of Chemical Technology/Kirk-Othmer, vol. 9*, ed. J. I. Kroschwitz, Wiley, New York, 1988, p. 759.
30 Public domain software to be downloaded from http://rsb.info.nih.gov/ij (National Institutes of Health).
31 J. R. Lakowicz, *Principles of Fluorescence Spectroscopy, 2nd edn*, Kluwer Academic/Plenum Publishers, New York, 1999.
32 H. P. Klug and L. E. Alexander, *X-Ray Diffraction Procedures for Polycrystalline and Amorphous Materials, 2nd edn*, John Wiley & Sons, New York, 1974.
33 L. L. Beecroft and C. K. Ober, *Chem. Mater.*, 1997, **9**, 1302–1317.
34 J. M. Alia, H. G. M. Edwards and B. M. Kiernan, *J. Raman Spectrosc.*, 2004, **35**, 111–118.
35 L. Guo, S. H. Yang, C. L. Yang, P. Yu, J. N. Wang, W. K. Ge and G. K. L. Wong, *Appl. Phys. Lett.*, 2000, **76**, 2901–2903.
36 R. D. Yang, S. Tripathy, Y. T. Li and H. J. Sue, *Chem. Phys. Lett.*, 2005, **411**, 150–154.
37 R. N. Bhargava, *J. Lumin.*, 1996, **70**, 85–94.
38 S. W. Buckner, R. L. Konold and P. A. Jelliss, *Chem. Phys. Lett.*, 2004, **394**, 400–404.
39 P. V. Kamat, *Pure Appl. Chem.*, 2002, **74**, 1693–1706.
40 A. van Dijken, J. Makkinje and A. Meijerink, *J. Lumin.*, 2001, **92**, 323–328.
41 W. Caseri, *Macromol. Rapid Commun.*, 2000, **21**, 705–722.
42 A. van Dijken, E. A. Meulenkamp, D. Vanmaekelbergh and A. Meijerink, *J. Lumin.*, 2000, **90**, 123–128.
43 S. Sakohara, M. Ishida and M. A. Anderson, *J. Phys. Chem. B*, 1998, **102**, 10169–10175.
44 S. Monticone, R. Tufeu and A. V. Kanaev, *J. Phys. Chem. B*, 1998, **102**, 2854–2862.
45 G. Rodríguez-Gattorno, P. Santiago-Jacinto, L. Rendon-Vázquez, J. Németh, I. Dékány and D. Díaz, *J. Phys. Chem. B*, 2003, **107**, 12597–12604.
46 L. Poul, N. Jouini and F. Fievet, *Chem. Mater.*, 2000, **12**, 3123–3132.
47 E. Hosono, S. Fujihara, T. Kimura and H. Imai, *J. Colloid Interface Sci.*, 2004, **272**, 391–398.
48 P. Schindler, H. Althaus and W. Feitknecht, *Helv. Chim. Acta*, 1964, **47**, 982–991.
49 C. H. Liang, Y. Shimizu, M. Masuda, T. Sasaki and N. Koshizaki, *Chem. Mater.*, 2004, **16**, 963–965.
50 M. M. Demir, M. Memesa, P. Castignolles and G. Wegner, *Macromol. Rapid Commun.*, 2006, **27**, 763–770.